arXiv:1401.5622v2 [quant-ph] 4 Feb 2015

Superconducting quantum node for entanglement and storage of microwave radiation

E. Flurin,[1] N. Roch,[1] J.D. Pillet,[1,2] F. Mallet,[1] and B. Huard[1,*]

[1] *Laboratoire Pierre Aigrain, Ecole Normale Supérieure-PSL Research University, CNRS, Université Pierre et Marie Curie-Sorbonne Universités, Université Paris Diderot-Sorbonne Paris Cité, 24 rue Lhomond, 75231 Paris Cedex 05, France*

[2] *Collège de France, 11 place Marcelin Berthelot, 75005 Paris, France*

(Dated: February 5, 2015)

Superconducting circuits and microwave signals are good candidates to realize quantum networks, which are the backbone of quantum computers. We have realized a quantum node based on a 3D microwave superconducting cavity parametrically coupled to a transmission line by a Josephson ring modulator. We first demonstrate the time-controlled capture, storage and retrieval of an optimally shaped propagating microwave field, with an efficiency as high as 80 %. We then demonstrate a second essential ability, which is the timed-controlled generation of an entangled state distributed between the node and a microwave channel.

Microwave signals are a promising resource for quantum information processing. Coupled to various quantum systems [1–4] they could realize quantum networks for continuous variable states, in which entangled information is processed by quantum nodes and distributed through photonic channels [5, 6]. The quantum nodes should generate and distribute microwave entangled fields while controlling their emission and reception in time. Superconducting circuits are able to generate entanglement [7–10] and quantum memories provide control in time as demonstrated in emerging implementations in the microwave domain using spin ensembles [11–13], superconducting circuits [14, 15] or mechanical resonators [16, 17]. Here, we present a superconducting device both able to store and generate entangled microwave radiations shared between a memory and a propagating mode. It is based on the Josephson ring modulator [18, 19] that enables to switch dynamically on or off the coupling between a low-loss cavity and a transmission line by frequency conversion. We demonstrate the time-controlled capture, storage and retrieval of a propagating coherent state in a long lived electromagnetic mode. Exploiting the versatility of this circuit, we then demonstrate the timed-controlled generation of an Einstein-Podolsky-Rosen (EPR) state distributed between the quantum memory and a propagating wavepacket. These new capabilities pave the way for complex quantum communication and quantum computing protocols by means of photonic channels in the microwave domain.

The superconducting node is made of three components: a memory, a buffer and a parametric coupler linking them. The memory is the fundamental mode $\hat{m}$ at frequency $f_m = 7.80$ GHz of a low-loss 3D superconducting cavity cooled down to 40 mK (Fig. 1). The buffer is the fundamental mode $\hat{a}$ at frequency f_a of an on-chip resonator and is the only component directly coupled to the network channels with propagating modes $\hat{a}_{in/out}$. The large coupling rate $\kappa_a = (20\ \text{ns})^{-1}$ between buffer and channel ensures fast communication

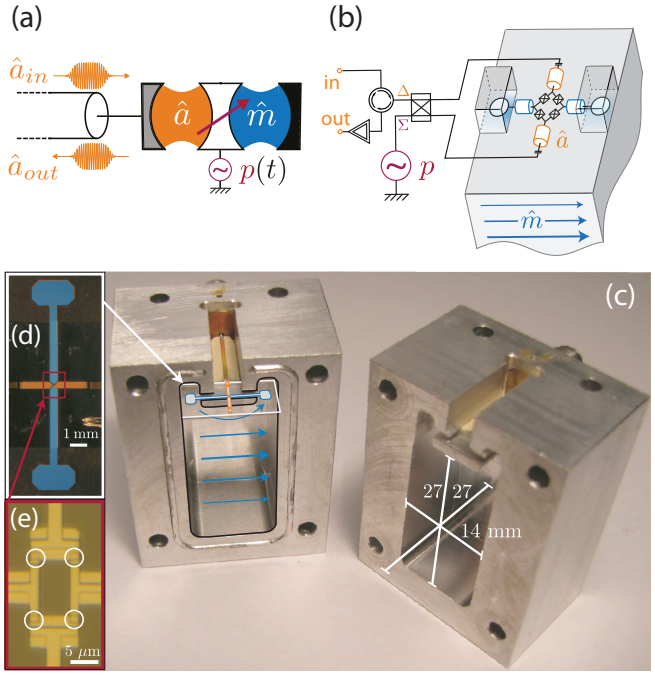

Figure 1: (a) Schematic of the experimental setup. A high-Q memory mode $\hat{m}$ is parametrically coupled to a low-Q buffer mode $\hat{a}$, hence to input/output propagating modes $\hat{a}_{in}$ and $\hat{a}_{out}$, depending on the pump amplitude p. (b),(c) Schematics and picture of the device. The on-chip circuit couples to a 3D superconducting cavity via antennas. The blue arrows represent the polarization of the fundamental mode TE 110 in the cavity. The Josephson ring and buffer resonator are on-chip. The differential mode (Δ) couples with the buffer mode while the common mode (Σ) is used for addressing the pump. (d) Picture of the aluminum circuit fabricated on a c-plane sapphire substrate. The antennas (blue) and the buffer microstrip resonator (orange) are highlighted in false color. (e) Optical microscope image of the Josephson ring at the crossing between antennas and buffer resonator. The Josephson junctions are circled in white.

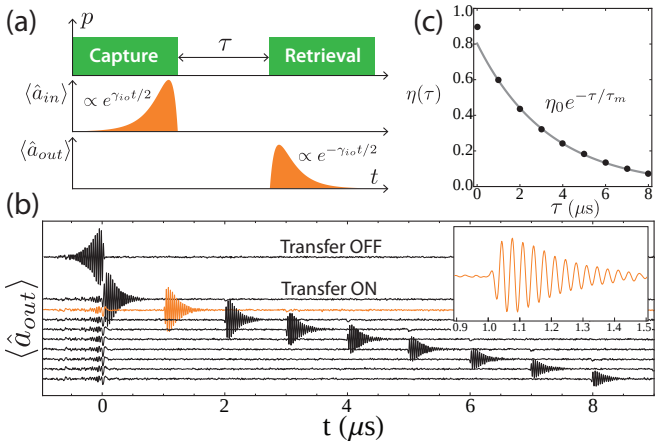

Figure 2: (a) Capture, store and release protocol. Pulse sequences for the pump field p (green) at the difference frequency $f_p = f_a - f_m$, the input field a_{in} and the resulting output field a_{out} (orange). The temporal shape of the input field is chosen in order to optimize the capture efficiency. (b) Time traces of the amplitude of the output field down converted to 40MHz and averaged 6×10^4 times. The top trace is measured without pump and reveals the optimized input signal. The following traces correspond to the sequence of (a) with increasing delay τ between capture and retrieval from 0 μs to 8 μs. The trace at $\tau = 1$ μs is magnified for clarity as an inset. (c) Dots: retrieval efficiency η as function of delay τ. η is defined as the ratio of the retrieved energy normalized to the input energy. Plain line: exponential decay $\eta_0 e^{-\tau/\tau_m}$ characterizing the memory lifetime. Best fit obtained for $\eta_0 = 80$ % and $\tau_m = 3.3$ μs.

compared to decoherence. The memory and buffer are parametrically coupled through a ring of four Josephson junctions pumped with a classical control field p at frequency f_p. The magnetic flux through the ring allows to tune f_a between 8.7 and 9.6 GHz. As described in previous works [20], the ring performs three-wave-mixing and $H_{mix} = \hbar\chi(\hat{a}+\hat{a}^\dagger)(\hat{m}+\hat{m}^\dagger)(p+p^*)$. The device can be operated in two distinct ways depending on the pump frequency. For $f_p = |f_a - f_m|$, the device operates as a converter [18, 21]. In the rotating wave approximation (RWA) and with $p > 0$ the term $H_{conv} = \hbar\chi p(\hat{a}^\dagger\hat{m}+\hat{a}\hat{m}^\dagger)$ provides a tunable coupling rate χp with frequency conversion between the buffer and memory modes. Conversely, for $f_p = f_a + f_m$, the RWA leads to the parametric down-conversion Hamiltonian $H_{pd} = \hbar\chi p(\hat{a}^\dagger\hat{m}^\dagger+\hat{a}\hat{m})$. The device then operates as an entanglement generator [9]. Starting from the vacuum state, an EPR state is distributed between the propagating mode $\hat{a}_{out}$ and memory mode $\hat{m}$. These properties offer a striking resemblance with memories based on mechanical resonators. However, unlike the latter, superconducting circuits do not require extra cooling steps and offer three orders of magnitude larger input/output rates [16, 17].

In order to demonstrate the performances of the memory, one can first capture and retrieve a propagating classical field. Depending on its temporal shape, the pump amplitude has to be shaped appropriately in order to maximize the capture efficiency, while taking care of the resonance frequency shifts that are induced by the pump power [22–24]. In this first experiment, we used the easier dual approach of optimizing the temporal shape of an incoming coherent state so that it is captured by a square pump pulse turning off at time $t = 0$ (Fig. 2a) similarly to Ref. [14, 15]. The optimal shape corresponds to the time-reverse of a signal retrieved from an initially occupied memory [15, 24]. It is an exponential rise in power (Fig. 2), which defines the input/output rate γ_{io} of the quantum node. Note that, due to the presence of the buffer, the pulse finally turns off smoothly on the scale of κ_a^{-1} [24]. The amplitude of the pump pulse was chosen in order to maximize the input/output rate to γ_{io}. Indeed, for large enough pump powers such that $\chi p > \kappa_a/4$ the modes $\hat{a}$ and $\hat{m}$ hybridize and the input/output rate saturates to its upper limit [24]. In practice, the finite coupling capacitance between the 3D cavity and the antennas (Fig. 1) prevents γ_{io} to reach an upper limit of $\kappa_a/2$ and we found a three times lower rate $\gamma_{io} \approx (110\text{ ns})^{-1}$ instead [24]. It is worthwhile to note that, although the memory has a finite lifetime, the frequency conversion between modes m and a ensures that the input/output rate is exactly zero $\gamma_{io} = 0$ when the pump is turned off, leading to an infinite on/off ratio. Besides, the device being non-resonant with the conversion operating frequency $f_p = f_a - f_m \approx 1.5$ GHz, the transfer rate can be varied much faster than κ_a.

The amplitude $\langle\hat{a}_{out}\rangle$ of the mode coming back from the device is measured for several pump pulse sequences (Fig. 2b). In a first control measurement (top trace), the pump is kept turned off such that the measurement corresponds to the directly reflected incoming pulse [33]. In the following measurements (traces below) the pump is turned on before time 0 and after time τ (Fig. 2a). A small part of the incoming pulse energy is reflected, at least 5 % according to the average trace in Fig. 2a, while it is sent at $t < 0$ indicating the efficient absorption of this pulse shape. When the pump is turned back on after a delay τ, the device releases the captured state back in the transmission line as can be seen in Fig. 2b. Note that the chosen temporal shape of the incoming signal is indeed the time reverse of these pulses up to an amplitude rescaling, which corresponds to the efficiency of the memory. Calculating the memory efficiency η, which is the ratio between the retrieved pulse energy and the incoming pulse energy leads to an exponential decay as a function of delay time $\eta(\tau) = \eta_0 e^{-\tau/\tau_m}$ (Fig. 2c). The memory lifetime $\tau_m = 3.3$ μs is much larger than γ_{io}^{-1} but limited by unidentified losses in the 3D cavity coupled to the antennas. The much smaller decay rates achieved in similar 3D cavities [26] leave room for improvement in the future. Note that the anomalously large efficiency at zero delay $\eta(0) > \eta_0 = 80$ % should not be consid-

ered as a useful efficiency. Indeed, part of the retrieved energy right after time $t = 0$ corresponds in fact to the decay of the part of the signal that was not stored in the memory mode and stayed in the buffer mode instead. Note that the memory withstands large signal amplitudes, since there are here 10 photons on average in the incoming wavepacket. Besides the outgoing phase is identical to that of the incoming pulse. The phase coherence properties of the device at the single photon level are demonstrated below. Finally, the number of operations that can be performed by the memory within its lifetime is limited by the time-bandwidth product $\gamma_{io}\tau_m = 30$. This combination of large memory efficiency and time-bandwidth product makes this device a state of the art quantum memory [15, 27].

Promisingly, the device cannot only be used as a memory but also as an entanglement generator. In a second experiment, we demonstrate the generation of an EPR state distributed between the propagating mode $\hat{a}_{out}$ and the memory mode. Note that this experiment has been performed during another cooldown of the same device for which the memory lifetime was slightly degraded to $\tau_m = 2.3$ μs. Starting from the vacuum state both in the memory and in the mode $\hat{a}_{out}$, a pulse at pump frequency $f_p = f_a + f_m = 17.28$ GHz produces a two-mode squeezed vacuum state $|Sq\rangle = e^{iH_{pd}\tau/\hbar}|0\rangle_a|0\rangle_m = \cosh(r)^{-1}\sum \tanh(r)^n |n\rangle_a |n\rangle_m$ where the squeezing parameter r increases with the pump pulse amplitude [9]. The entanglement between memory and propagating modes can be demonstrated by measuring the correlations between the fluctuations of their mode quadratures, and showing that there is more correlation than allowed by classical physics [7, 8, 10]. The quadratures of both modes can be measured using the same detector on line a provided that the memorized field is released into the transmission line at a later time.

The pulse sequence used in the experiment (Fig. 3a) starts by a square pump pulse at $f_p = f_a + f_m = 17.28$ GHz during 500 ns that generates an EPR state. While one part of the pair is stored in the memory, the other part propagates in the transmission line, is amplified by a low-noise amplifying detection setup and recorded using fast digital heterodyne detection based on a Field Programmable Gate Array (FPGA) [7, 28]. After a delay $\tau = 200$ ns, a square pulse is applied on the pump field at $f_p = f_a - f_m$ with an amplitude such that the output rate is γ_{io} and lasting for 500 ns. This pulse releases the memory field which is then amplified and measured using the heterodyne detection setup. At the end of a sequence, the four mode quadratures $\hat{X}_a$, $\hat{P}_a$, $\hat{X}_m$ and $\hat{P}_m$ have been measured (defining $\hat{X}_m \equiv (\hat{m}+\hat{m}^\dagger)/2$ and $\hat{P}_m \equiv (\hat{m}-\hat{m}^\dagger)/2i$).

In order to perform a tomography of the entangled state, this sequence is repeated 4×10^7 times. The FPGA generates six histograms giving the probability distribution of measurement outcomes as a function of every pair

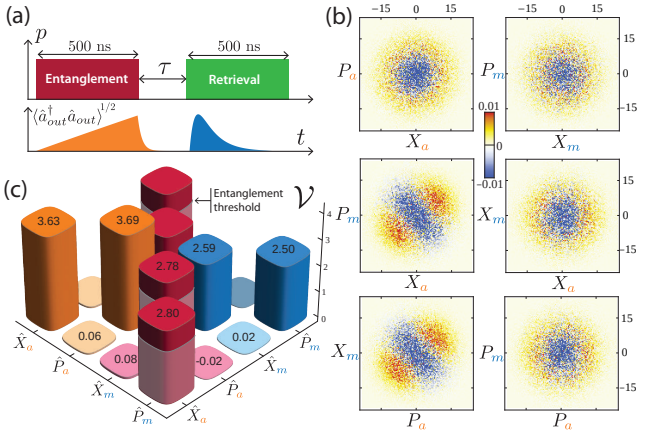

Figure 3: Entanglement between memory and propagating mode. (a) Scheme of the pulse sequence. Top: pump amplitude p is shown in red for $f_p = f_a + f_m$ and in green for $f_p = f_a - f_m$. Bottom: output noise amplitude in time. (b) Difference between measured quadrature histograms with pump turned on and off for all pairs of quadratures for a delay $\tau = 200$ ns. The quadratures are calibrated separately (see text) so that the vacuum fluctuations would result in $\langle X^2_{a,m}\rangle = \langle P^2_{a,m}\rangle = 1/4$. The color scale is in units of the maximal value of the histogram with pump off. (c) Resulting two-mode covariance matrix. The convention used is such that the vacuum state corresponds to the unity matrix. The 2×2 block-diagonal matrices in orange and blue represent the single mode $\hat{a}$ and $\hat{m}$ covariance matrices. The off-diagonal matrices in red represent the correlations between modes. The typical error on the matrix terms is 0.07. Correlations go beyond the greyed regions which demonstrates entanglement.

of mode quadratures (see phase space in Fig. 3b). The total acquisition and processing time amounts to 5 minutes. In practice, the resulting histograms are dominated by the uncorrelated noise of the detection setup. It is possible to cancel the contribution of this noise background by turning off the pump in another pulse sequence and subtracting the corresponding histograms to the original ones (Fig. 3b) [7, 28]. In order to avoid gain drifts, on and off pump sequences are performed every 30 s.

In the single-mode histograms along $(\hat{X}_a, \hat{P}_a)$ and along $(\hat{X}_m, \hat{P}_m)$, a phase-independent increase in the fluctuations is observed. This corresponds to the thermal state produced in a mode by tracing out the EPR state $|S_q\rangle$ on the other mode. On the contrary, the histograms along the quadratures of two different modes $(\hat{X}_a, \hat{P}_m)$ and $(\hat{P}_a, \hat{X}_m)$ exhibit large values along a diagonal indicating strong correlations between modes. For instance, the measurement outcomes X_a and P_m are likely to have the same sign. These correlations need to be characterized quantitatively in order to demonstrate whether or not they are non-classical.

The correlations can be calibrated using the known variance of the single mode quadratures. Indeed, for mode a, the thermal state corresponds to amplified vac-

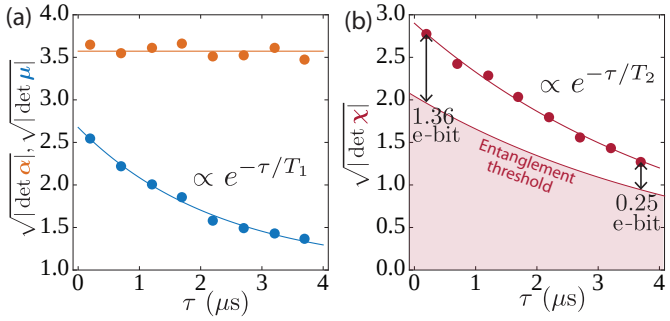

Figure 4: Covariance matrix and entanglement as a function of the storage time τ. (a) Dots: diagonal terms of the covariance matrix $\mathcal{V}$ giving the energy of each mode. Lines: average value (for α) and exponential fit (for β). The decay rate of the terms in β gives the energy relaxation time $T_1 = 2.3 \pm 0.1$ μs. (b) Dots: Off-diagonal amplitudes in $\mathcal{V}$ representing the coherence between memory and propagating modes. Line: exponential fit, whose rate sets the decoherence time $T_2 = 4.5 \pm 0.1$ μs. Correlations above the entanglement threshold demonstrate entanglement between memory and propagating modes. The threshold decays in time because of the single mode noise decay in (a). Logarithmic negativity E_N measuring the entanglement between modes is indicated for the two limit times.

uum fluctuations with a power gain $\cosh(2r)$ resulting in a variance for both quadratures $\Delta X_a^2 = \Delta P_a^2 = \cosh(2r)/4$. Note that we assume that the field is in the vacuum at thermal equilibrium with the refrigerator temperature 45 mK $\ll hf/k_B \approx 0.4$ K [34]. The calibration then comes down to determining the gain $\cosh(2r)$ precisely. This can be done by storing a small coherent field (about 1 photon on average) in the memory and measuring the output amplitudes with and without applying the entangling 500 ns pump tone at $f_p = 17.28$ GHz before release [9]. The entangling pulse effectively amplifies the coherent field with an amplitude gain $\cosh(r)$ which is here found to be equal to 1.51.

One can then calculate the covariance matrix $\mathcal{V}$ of the two mode state (Fig. 3c), which fully characterizes the EPR state since it is Gaussian with zero mean [29]. The FPGA processes 4×10^7 pulse sequences in 5 minutes so that $\mathcal{V}$ is calculated with minimal post-processing [7, 10, 24, 30]. In a coordinate system where $\mathbf{x} = \{\hat{X}_a, \hat{P}_a, \hat{X}_m, \hat{P}_m\}$, one defines $\mathcal{V}_{ij} = 2(\langle x_i x_j + x_j x_i\rangle - 2\langle x_i\rangle\langle x_j\rangle)$. Physically, it is meaningful to decompose it in four 2×2 block matrices.

$$\mathcal{V} = \begin{pmatrix} \boldsymbol{\alpha} & \boldsymbol{\chi} \\ \boldsymbol{\chi}^T & \boldsymbol{\mu} \end{pmatrix}. \quad (1)$$

The diagonal blocks $\boldsymbol{\alpha}$ and $\boldsymbol{\mu}$ are the single-mode covariance matrices for $\hat{a}$ and $\hat{m}$ respectively. Since an EPR state is thermal when disregarding the other mode, there is no correlation between quadratures X and P for a single mode and the variances ΔX^2 and ΔP^2 are almost equal. For mode a, by definition of the calibration process, one gets $\mathcal{V}_{11} \approx \mathcal{V}_{22} \approx \cosh(2r) = 3.66$ (Fig. 3c). The memory mode is less occupied because of losses at a rate τ_m^{-1} during the entanglement pulse and the waiting time $\tau = 200$ ns so that $\mathcal{V}_{33} \approx \mathcal{V}_{44} \approx 2.55$. Conversely, the off-diagonal blocks $\boldsymbol{\chi}$ correspond to the correlations between modes. In each block, the phase of the pump field was optimized to put all the weight of the correlations in the two terms $\mathcal{V}_{14} \approx \mathcal{V}_{23} \approx 2.79$. The amount of entanglement in the two mode state can be measured by the logarithmic negativity E_N. It corresponds to an upper bound for distillable entanglement [30]. Here, the memory and the propagating modes share $E_N = 1.36$ entangled bits (e-bits), which indeed demonstrates the ability of the device to generate and preserve entanglement between modes.

The experiment was repeated for various storage times τ (Fig. 3a). The typical amplitude $\sqrt{|\det\boldsymbol{\mu}|}$ of the memory mode terms in $\mathcal{V}$ decrease exponentially with τ (Fig. 4a) as expected from the experiment with coherent states in Fig. 2c. This leads to a relaxation time for the memory of $T_1 = 2.3 \pm 0.1$ μs in agreement with the memory lifetime τ_m measured using coherent states in the same cool down of the device. The small variations in the amplitude of the propagating mode $\sqrt{|\det\boldsymbol{\alpha}|}$ with τ give a sense of the measurement uncertainty (Fig. 4a). Interestingly, the two-mode correlations also decay exponentially (Fig. 4b). The corresponding characteristic time is the decoherence time $T_2 = 4.5 \pm 0.1$ μs of the memory. The fact that $T_2 \approx 2T_1$ demonstrates that energy relaxation dominates all decoherence mechanisms during the storage of a quantum state. The logarithmic negativity also decreases with τ as shown in Fig. 4b.

In conclusion, we have realized quantum node based on an hybrid 2D/3D superconducting circuit. The efficient capture, storage and retrieval of a coherent state was demonstrated. Moreover, the device permits the generation and storage of entangled states distributed between the node and photonics channels. The versatility of the device paves the way for complex quantum communication protocols in the microwave domain such as continuous variable quantum teleportation. Besides, it provides a useful resource for 3D cavities where the on-demand extraction of a field quantum state was needed. This could be used to implement readout and feedback in cavity networks or even quantum computation with the memory field itself [31]. Finally, superconducting qubits can easily be embedded in this device, therefore enabling the strong coupling between a qubit and a continuous variable entangled state, which leads to protected quantum memories [4] and even protected quantum computing with microwave fields [31, 32].

We thank Michel Devoret, Vladimir Manucharyan, Mazyar Mirrahimi and Pierre Rouchon for enlightening discussions and Landry Bretheau and Philippe Campagne-Ibarcq for proofreading. Nanofabrication has been made within the consortium Salle Blanche Paris

Centre. This work was supported by the EMERGENCES program from Ville de Paris under the project QUMOTEL and by the Idex ANR-10-IDEX-0001-02 PSL *. JDP acknowledges financial support from Michel Devoret.

* corresponding author: benjamin.huard@ens.fr

[1] S. Haroche and J. Raimond. Exploring the Quantum: Atoms, Cavities, and Photons. *Oxford Graduated Text* 616 (2006).

[2] R. J. Schoelkopf and S. M. Girvin. Wiring up quantum systems. *Nature* **451**, 664–9 (2008).

[3] Z.-L. Xiang, S. Ashhab, J. Q. You and F. Nori. Hybrid quantum circuits: Superconducting circuits interacting with other quantum systems. *Reviews of Modern Physics* **85**, 623–653 (2013).

[4] M. H. Devoret and R. J. Schoelkopf. Superconducting circuits for quantum information: an outlook. *Science (New York, N.Y.)* **339**, 1169–74 (2013).

[5] J. Cirac, P. Zoller, H. Kimble and H. Mabuchi. Quantum State Transfer and Entanglement Distribution among Distant Nodes in a Quantum Network. *Physical Review Letters* **78**, 3221–3224 (1997).

[6] H. J. Kimble. The quantum internet. *Nature* **453**, 1023–30 (2008).

[7] C. Eichler, D. Bozyigit, C. Lang, M. Baur, L. Steffen, J. M. Fink, S. Filipp and A. Wallraff. Observation of Two-Mode Squeezing in the Microwave Frequency Domain. *Physical Review Letters* **107**, 113601 (2011).

[8] C. M. Wilson, G. Johansson, A. Pourkabirian, M. Simoen, J. Johansson, T. Duty, F. Nori and P. Delsing. Observation of the dynamical Casimir effect in a superconducting circuit. *Nature* **479**, 376–379 (2012).

[9] E. Flurin, N. Roch, F. Mallet, M. H. Devoret and B. Huard. Generating Entangled Microwave Radiation Over Two Transmission Lines. *Physical Review Letters* **109**, 183901 (2012).

[10] E. P. Menzel, R. Di Candia, F. Deppe, P. Eder, L. Zhong, M. Ihmig, M. Haeberlein, A. Baust, E. Hoffmann, D. Ballester, K. Inomata, T. Yamamoto, Y. Nakamura, E. Solano, A. Marx and R. Gross. Path Entanglement of Continuous-Variable Quantum Microwaves. *Physical Review Letters* **109**, 250502 (2012).

[11] H. Wu, R. E. George, J. H. Wesenberg, K. Mø lmer, D. I. Schuster, R. J. Schoelkopf, K. M. Itoh, A. Ardavan, J. J. L. Morton and G. A. D. Briggs. Storage of Multiple Coherent Microwave Excitations in an Electron Spin Ensemble. *Physical Review Letters* **105**, 140503 (2010).

[12] Y. Kubo, I. Diniz, a. Dewes, V. Jacques, a. Dréau, J.-F. Roch, a. Auffeves, D. Vion, D. Esteve and P. Bertet. Storage and retrieval of a microwave field in a spin ensemble. *Physical Review A* **85**, 012333 (2012).

[13] S. Saito, X. Zhu, R. Amsüss, Y. Matsuzaki, K. Kakuyanagi, T. Shimo-Oka, N. Mizuochi, K. Nemoto, W. J. Munro and K. Semba. Towards Realizing a Quantum Memory for a Superconducting Qubit: Storage and Retrieval of Quantum States. *Physical Review Letters* **111**, 107008 (2013).

[14] Y. Yin, Y. Chen, D. Sank, P. J. J. OMalley, T. C. White, R. Barends, J. Kelly, E. Lucero, M. Mariantoni, A. Megrant, C. Neill, A. Vainsencher, J. Wenner, A. N. Korotkov, A. N. Cleland and J. M. Martinis. Catch and Release of Microwave Photon States. *Physical Review Letters* **110**, 107001 (2013).

[15] J. Wenner, Y. Yin, Y. Chen and R. Barends. Catching Shaped Microwave Photons with 99.4% Absorption Efficiency. *Physical Review Letters* **112**, 210501 (2014).

[16] T. A. Palomaki, J. W. Harlow, J. D. Teufel, R. W. Simmonds and K. W. Lehnert. Coherent state transfer between itinerant microwave fields and a mechanical oscillator. *Nature* **495**, 210–4 (2013).

[17] T. A. Palomaki, J. D. Teufel, R. W. Simmonds and K. W. Lehnert. Entangling Mechanical Motion with Microwave Fields. *Science (New York, N.Y.)* **342** (2013).

[18] N. Bergeal, F. Schackert, M. Metcalfe, R. Vijay, V. E. Manucharyan, L. Frunzio, D. E. Prober, R. J. Schoelkopf, S. M. Girvin and M. H. Devoret. Phase-preserving amplification near the quantum limit with a Josephson ring modulator. *Nature* **465**, 64 (2010).

[19] N. Bergeal, R. Vijay, V. E. Manucharyan, I. Siddiqi, R. J. Schoelkopf, S. M. Girvin and M. H. Devoret. Analog information processing at the quantum limit with a Josephson ring modulator. *Nature Physics* **6**, 296–302 (2010).

[20] B. Abdo, A. Kamal and M. Devoret. Nondegenerate three-wave mixing with the Josephson ring modulator. *Physical Review B* **87**, 014508 (2013).

[21] B. Abdo, K. Sliwa, F. Schackert, N. Bergeal, M. Hatridge, L. Frunzio A. D. Stone, and M. H. Devoret. Full coherent frequency conversion between two microwave propagating modes. *Physical Review Letters* **110**, 173902 (2013).

[22] I. Novikova, A. V. Gorshkov, D. F. Phillips, A. S. Sø rensen, M. D. Lukin and R. L. Walsworth. Optimal Control of Light Pulse Storage and Retrieval. *Physical Review Letters* **98**, 243602 (2007).

[23] E. Sete, E. Mlinar and A. Korotkov. Robust quantum state transfer using tunable couplers. *arXiv preprint arXiv:1411.7103* 23 (2014).

[24] *See Supplementary Material, which includes Ref. [25]*

[25] C. M. Caves, J. Combes, Z. Jiang and S. Pandey. Quantum limits on phase-preserving linear amplifiers. *Physical Review A* **86**, 063802 (2012).

[26] H. Paik, D. I. Schuster, L. S. Bishop, G. Kirchmair, G. Catelani, a. P. Sears, B. R. Johnson, M. J. Reagor, L. Frunzio, L. I. Glazman, S. M. Girvin, M. H. Devoret and R. J. Schoelkopf. Observation of High Coherence in Josephson Junction Qubits Measured in a Three-Dimensional Circuit QED Architecture. *Physical Review Letters* **107**, 240501 (2011).

[27] C. Simon *et al.* Quantum memories. *The European Physical Journal D* **58**, 1–22 (2010).

[28] C. Eichler, D. Bozyigit and A. Wallraff. Characterizing quantum microwave radiation and its entanglement with superconducting qubits using linear detectors. *Physical Review A* **86**, 032106 (2012).

[29] S. L. Braunstein and P. van Loock. Quantum information with continuous variables. *Reviews of Modern Physics* **77**, 513–577 (2005).

[30] G. Adesso and F. Illuminati. Gaussian measures of entanglement versus negativities: Ordering of two-mode Gaussian states. *Physical Review A* **72**, 032334 (2005).

[31] Z. Leghtas, G. Kirchmair, B. Vlastakis, R. J. Schoelkopf, M. H. Devoret and M. Mirrahimi. Hardware-Efficient Autonomous Quantum Memory Protection. *Physical Review Letters* **111**, 120501 (2013).

[32] M. Mirrahimi, Z. Leghtas, V. V. Albert, S. Touzard, R. J. Schoelkopf, L. Jiang and M. H. Devoret. Dynamically protected cat-qubits: a new paradigm for universal quantum computation. *New Journal of Physics* **16**, 045014 (2014).

[33] Note that the signal is 20 MHz out of resonance with the buffer mode when the pump is turned off, so that the reflected power is identical to the incoming power.

[34] We have consistently found less than 0.5 % of excitation in 3D modes with similar setups and cavities using a 3D transmon qubit as a photocounter.